

1                   **Enabling Smart Dynamical Downscaling of Extreme**  
2                   **Precipitation Events with Machine Learning**

3                   **Xiaoming Shi<sup>1,2</sup>**

4                   <sup>1</sup>Division of Environment and Sustainability, Hong Kong University of Science and Technology

5                   <sup>2</sup>Department of Civil and Environmental Engineering, Hong Kong University of Science and Technology

6                   **Key Points:**

- 7                   • Dynamical downscaling at  $\sim 1$  km resolution produces reliable estimations of extreme  
8                   rainfall but is computationally expensive.  
9                   • Machine learning (ML) makes smart dynamical downscaling (SDD) possible, where ML  
10                  models filter out irrelevant large-scale patterns.  
11                  • We demonstrate that SDD can be enabled by deep neural networks, which do not  
12                  necessarily have to involve sophisticated structures.

## Abstract

The projection of extreme convective precipitation by global climate models (GCM) exhibits significant uncertainty due to coarse resolutions. Direct dynamical downscaling (DDD) of regional climate at kilometer-scale resolutions provides valuable insight into extreme precipitation changes, but its computational expense is formidable. Here we document the effectiveness of machine learning in enabling smart dynamical downscaling (SDD), which selects a small subset of GCM data to conduct downscaling. Trained with data for three subtropical/tropical regions, convolutional neural networks (CNNs) can retain 92% to 98% of extreme precipitation events (rain intensity higher than the 99th percentile) while filtering out 88% to 95% of circulation data. When applied to two different reanalysis data sets, the CNNs' skill in retaining extremes decreases modestly in subtropical regions but sharply in the deep tropics. Nonetheless, one of the CNNs can still retain 62% of all extreme events in the deep tropical region in the worst case.

## Plain Language Summary

Climate scientists use supercomputers to simulate the climate and predict how it may change under global warming. Extreme precipitation, which can disrupt society by causing disasters like floods and landslides, is of great interest in climate studies. However, replicating severe rainstorms on a supercomputer, especially the storms in tropical and subtropical areas, is not easy. Because those rainstorms often contain fine-scale details that cannot be represented confidently without extensive computational resources. If we use computationally affordable computer models to simulate those rainstorms, we obtain results with substantial uncertainties. If we use computationally expensive ones, we cannot simulate many scenarios and cannot be confident about the results. The power of machine learning in pattern recognition is here used to help modelers use their computational resources more efficiently. Instead of simulating all kinds of weather events, including unimportant ones, at high resolutions, we use machine learning algorithms to search coarse resolution climate data for those large-scale weather patterns that are more likely to cause severe rainstorms. Then modelers can make more efficient use of supercomputing resources by simulating severe weather events only and advance our understanding of them.

## 1 Introduction

Extreme precipitation events often disrupt society by causing disasters such as floods and landslides. Thus, predicting the response of precipitation extremes to global warming is crucial for our adaptation to climate change. Climate models agree well with each other on the potential response of extreme extratropical precipitation to global warming, but their results for subtropical and tropical extremes diverge (O'Gorman & Schneider, 2009). Predicting such changes is not straightforward, because the performance of numerical simulation of extreme precipitation is sensitive to model resolution (Li et al., 2018; Van Der Wiel et al., 2016), and grid spacings of current-generation climate models are still at coarse  $\sim 1^\circ$  resolutions. Previous studies have demonstrated that to accurately predict future changes in extreme precipitation events, especially those associated with severe convection, it is necessary to resolve local storm dynamics with kilometer-scale grid spacings, which are the so-called convection-permitting resolution (Kendon et al., 2014, 2017). Such a high resolution is necessary not only because of the small spatial scale of convective cells, but also because the essential roles played by the interaction between convection and large-scale dynamics, air-sea coupling, and topographic forcing in determining the intensity of extreme events (Nie et al., 2016; Kendon et al., 2017; Rainaud et al., 2017).

Modelers have been attempting to refine the resolution of global climate models, but the current highest resolution is only  $\sim 25$  km (Haarsma et al., 2016). A direct dynamical downscaling (DDD) approach has been adopted in the regional climate simulations at convection-permitting resolutions. Valuable findings have been obtained due to improved representation of

63 fine-scale processes, but DDD at the convection-permitting resolution has a very high demand  
64 on computational resources (Prein et al., 2015).

65 Is there a way to avoid the expensive computational cost of long-term DDD but still allow  
66 a convection-permitting resolution? This question is the core problem we want to address in  
67 this study. When our concern is not the mean climate but instead a special kind of weather  
68 (e.g., extreme precipitation), we can save a tremendous amount of computational resources if  
69 we do not have to perform the DDD for every day of an extended period. In this study, we  
70 harness the power of machine learning to fulfill the goal of selecting a small subset of GCM  
71 data for the dynamic downscaling of extreme precipitation events. We call this strategy smart  
72 dynamical downscaling (SDD).

73 Machine learning has been increasingly used in geoscience in recent years. In the atmo-  
74 spheric science community, it has applied to real-time nowcasting (Han et al., 2017; McGovern  
75 et al., 2017), physical parameterization (Brenowitz & Bretherton, 2019; Gagne et al., 2020),  
76 and weather forecasting (Weyn et al., 2019; Chattopadhyay et al., 2020). In the area of ex-  
77 treme precipitation, previous authors have documented the potential of machine learning in  
78 identifying the synoptic-scale patterns responsible for extreme events (Agel et al., 2018; Con-  
79 ticello et al., 2018; Knighton et al., 2019). However, they mostly focused on synoptic-scale  
80 weather patterns in the extratropics. The current study differs from previous ones in that we  
81 intentionally chose subtropical and tropical regions for potential applications on convective  
82 rainfall, which might be more difficult to capture based on large-scale circulation. Also, be-  
83 cause the purpose of this study is to evaluate the potential of SDD, we used machine learning  
84 for the classification problem of circulation patterns, instead of attempting to predict the exact  
85 precipitation amount like other statistical downscaling studies (e.g., Sachindra et al., 2018).

86 In this study, we evaluated three machine learning models, a dual support vector ma-  
87 chine (SVM) model, an 8-layer deep convolutional neural network (CNN), and a sophisticated  
88 58-layer deep CNN, in classifying circulation patterns responsible for 6-hourly precipitation  
89 extremes. The performance of these machine learning models with increasing complexity is  
90 documented, and we found the deep CNN with a simpler structure appears to suffice for SDD.

## 91 2 Data and Methods

### 92 2.1 Reanalysis and Satellite Data

93 In this study, we train machine learning models with reanalysis data of circulation and  
94 satellite data of 6-hourly precipitation. Our study focused on the areas surrounding three  
95 Asian cities, Hong Kong (HK), Manila (MN), and Singapore (SG). The extreme rainfall of these  
96 regions is often related to intense convection, though not always. Their different latitudes can  
97 contrast applicability of the methodology developed here for subtropical and tropical climate.

98 The precipitation data we used is the final precipitation, Level 3 data of the Integrated  
99 Multi-satellitE Retrievals for Global Precipitation Measurement (GPM IMERG; Huffman et  
100 al., 2019). This data set has  $0.1^\circ$  spatial resolution and 30 min temporal resolution originally.  
101 We used the data set between the period of June 2000 to May 2019. Because the reanalysis  
102 data has a 6-hour temporal resolution, we average the original data in time to get the mean  
103 precipitation rate in 6-hour intervals. We also used area averaging of the precipitation data  
104 to coarse-grain the data onto a  $0.5^\circ \times 0.5^\circ$  grid to ignore sporadic events that affect only a  
105 small area.

106 Multiple reanalysis data sets were used in the training and evaluation of machine learning  
107 models. For the training of SVM models, we use the NCEP/NCAR Global Reanalysis Products  
108 (Kalnay et al., 1996) to represent the state of the atmospheric circulation. This data set has  
109  $2.5^\circ \times 2.5^\circ$  horizontal resolution. We use data on eight pressure levels between 1000 hPa to  
110 300 hPa. The variables we chose to depict the large-scale circulation include 7 three dimen-  
111 sional variables: geopotential height, relative humidity, temperature,  $u$ - and  $v$ -components of

112 horizontal wind, vertical (pressure) velocity, and vorticity, in addition to 3 single-level variables  
 113 — surface pressure, tropopause pressure, and precipitable water. The temporal resolution of  
 114 the reanalysis data is 6 hours. The circulation variables were normalized with the mean and  
 115 standard deviation at each level. The precipitation data from reanalysis was not used because  
 116 they represent precipitation from large-scale circulation and have a significant bias. Sup-  
 117plementary Figure S1 shows that precipitation data from the reanalysis data suggest wrong  
 118 timing and intensities compared with GPM observation.

119 An SVM takes the circulation data in the  $15^\circ \times 15^\circ$  square region centered at one of  
 120 the three cities as input. Each time slice is categorized as producing “significant rain” or “no  
 121 significant rain” (with the 30th percentile of rain rate as the threshold), “light rain” or “heavy  
 122 rain” (with the 60th, 70th, or 80th percentile as the threshold, see Section 3.1), based on  
 123 next-6-hour precipitation in the  $0.5^\circ \times 0.5^\circ$  cell centered at the same city. The SVMs were  
 124 trained to classify the large-scale circulation patterns accordingly.

125 For the training of deep neural networks (RaNet and RxNet described below), we used  
 126 the NCEP FNL operational analysis data on  $1^\circ \times 1^\circ$  grids (NCEP/NWS/NOAA, 2000). The  
 127 NCEP/NCAR reanalysis data was not used for the training of CNNs, because its coarse  
 128 resolution hampers the use of multiple convolutional layers. To reduce the computational cost  
 129 in training the CNNs, we only used five variables (geopotential height, temperature, relative  
 130 humidity, and  $u$ - and  $v$ -components of wind) on six pressure levels (300, 500, 700, 850, 925  
 131 and 1000 hPa). Normalization procedure depends on the choice of network structures (see  
 132 Section 2.3).

133 When training the deep neural networks, we included the precipitation data for about  
 134 40 to 50 additional  $0.5^\circ \times 0.5^\circ$  grid cells surrounding each of those three cities (and the  
 135 accompanying circulation data) to obtain more samples, which helps prevent overfitting. The  
 136 extent of the surrounding areas was determined by applying the trained SVMs to new nearby  
 137 grid cells and evaluate the performance of the SVMs. The relatively high performance suggests  
 138 the weather patterns governing precipitation at the new location are similar to those at the  
 139 original training location. Thus, it is appropriate to include the new grid cell’s data to increase  
 140 the total sample size. The exact extent of the selected HK, MN, and SG regions is shown in  
 141 Supplementary Figure S2, with selection threshold provided in the caption of Fig. S2.

142 6-hourly precipitation data of each  $0.5^\circ \times 0.5^\circ$  cell within a selected region are used to  
 143 categorize the corresponding time and location as producing “extreme rain” or “non-extreme  
 144 rain” (with the 90th percentile of rain rate as the threshold). The input data for the neural  
 145 networks are the FNL data spline interpolated onto  $12^\circ \times 12^\circ$  square regions, which are  
 146 centered at each of the  $0.5^\circ \times 0.5^\circ$  rain data cells and have  $1^\circ \times 1^\circ$  resolution (Supplementary  
 147 Figure S3).

148 Finally, to evaluate the sensitivity of the trained neural networks to potential model biases  
 149 in climate simulations. We evaluated the performance of the FNL-trained neural networks with  
 150 another two reanalysis data sets, ERA5 (Copernicus Climate Change Service, 2017) and JRA-  
 15155 (Japan Meteorological Agency, 2013), which were spline interpolated onto  $1^\circ \times 1^\circ$  grid and  
 152 used by the FNL-trained CNNs to make predictions. Leading-order model “biases” in the ERA5  
 153 and JRA-55 data were removed by adjusting their mean and root-mean-square perturbation  
 154 amplitude at each pressure level to be the same as FNL data.

## 155 2.2 Support Vector Machine

156 An SVM is a machine learning model for classification problems (Cristianini et al., 2000).  
 157 At its core, SVMs find a hyperplane in the feature space of data and separate points in the  
 158 feature space into different groups. The hyperplane in feature space is defined as the set of  
 159 points  $x$  satisfying

$$160 \quad \mathbf{w} \cdot \mathbf{x} + b = 0 \quad (1)$$

161 The vector  $\mathbf{w}$  and scalar  $b$  for the best hyperplane are determined by an optimization pro-  
 162 cedure that maximizes the margin between two classes in the feature space. For a linearly  
 163 separable problem,  $\mathbf{w}$  and  $b$  are entirely determined by those sample points that are closest  
 164 to the best hyperplane. Those sample points are called support vectors. When data are not  
 165 linearly separable, one can use a soft margin technique to allow a small number of misclassified  
 166 instances.

167 Furthermore, in nonlinear classification problems, it is common to use a kernel function  
 168 to replace dot product for operating the optimization algorithm in a transformed feature space  
 169 implicitly. In our application, we used the Gaussian radial basis function,

$$170 \quad G(\mathbf{x}_i, \mathbf{x}_j) = \exp\left(-\frac{\|\mathbf{x}_i - \mathbf{x}_j\|^2}{2\sigma^2}\right) \quad (2)$$

171 where  $\sqrt{2}\sigma$  is called kernel scale. Besides  $\sigma$ , the other hyperparameter for training an SVM  
 172 is the box constraint which appears in the soft margin formula and determines the tolerance  
 173 level of misclassification.

174 We first attempted to select instances for extreme events by training a pair of SVMs. The  
 175 first SVM (SVM1) tells whether the circulation data of a time slice can produce “significant”  
 176 rainfall or not, with the 30th percentile of rain rate as the threshold. The subset of circulation  
 177 data, which SVM1 predicts to produce significant rain, is then adopted by the second SVM  
 178 (SVM2), which uses a higher percentile (60th, 70th, or 80th) as its threshold for “extremes”.  
 179 We found that this dual-SVM strategy can yield higher precision and recall than using a single  
 180 SVM to directly predict “extremes”.

181 MATLAB R2019b was used to train SVMs and the CNNs described below. The SVMs  
 182 were trained using Bayesian optimization to find out the best hyperparameters. Its performance  
 183 was evaluated with 10-fold cross-validation, in which input data set was partitioned into ten  
 184 subsets, and each subset was sequentially used as validation set while the other nine used for  
 185 training. Performance metrics are based on ten-time averages.

### 186 2.3 Convolutional Neural Network

187 In its essence, a neural network transforms the signal from one layer of neurons to the  
 188 next through a linear transformation and the use of a nonlinear activation function,

$$189 \quad \mathbf{z}^{[k]} = \mathbf{W}^{[k]}\mathbf{a}^{[k-1]} + \mathbf{b}^{[k]}, \quad \mathbf{a}^{[k]} = g^{[k]}(\mathbf{z}^{[k]}) \quad (3)$$

190 where  $\mathbf{a}^{[k]}$  is the activation of Layer  $k$ ,  $\mathbf{W}^{[k]}$  is a weight matrix, and  $\mathbf{b}^{[k]}$  is a bias vector.  $g^{[k]}$  is  
 191 a non-linear activation function. For Layer 0, the activation  $\mathbf{a}^{[0]}$  is the vector of input data  $\mathbf{x}$ . A  
 192 fully connected layer in a deep neural network connects every neuron in the previous layer to  
 193 every neuron in the current layer. A convolutional layer, by contrast, has multiple filters, which  
 194 are used to convolve a sub-block of the activation data from the previous layer and connect  
 195 that subset of neurons to a neuron in the current layer.

196 Two CNN structures are tested in this study (Fig. 1). They are motivated by the AlexNet  
 197 (Krizhevsky et al., 2012) and Xception (Chollet, 2017) models, respectively, which showed  
 198 excellent performance in computer vision competitions. This first CNN used in this study is  
 199 named as RaNet (motivated by AlexNet, Fig. 1a). It has 3 convolution layers and 5 fully  
 200 connected layers. Differing from the original AlexNet, RaNet here uses three-dimensional  
 201 filters in its convolutional layers; thus, its input layer has five channels (variables). By contrast,  
 202 RxNet (motivated by Xception, Fig. 1b) treats the data on each pressure level as one individual  
 203 variable; thus its input layer has 30 channels (5 variables  $\times$  6 levels). Such a design of RxNet  
 204 is used for closely following the original Xception model, which was applied to two-dimensional  
 205 images. RxNet is 58-layer deep and includes multiple residual connections.

206 Input data for RaNet are scaled perturbations. We define base-state profiles of geopo-  
 207 tential height and temperature as their climatological means and the base-state profiles for  $u$ ,

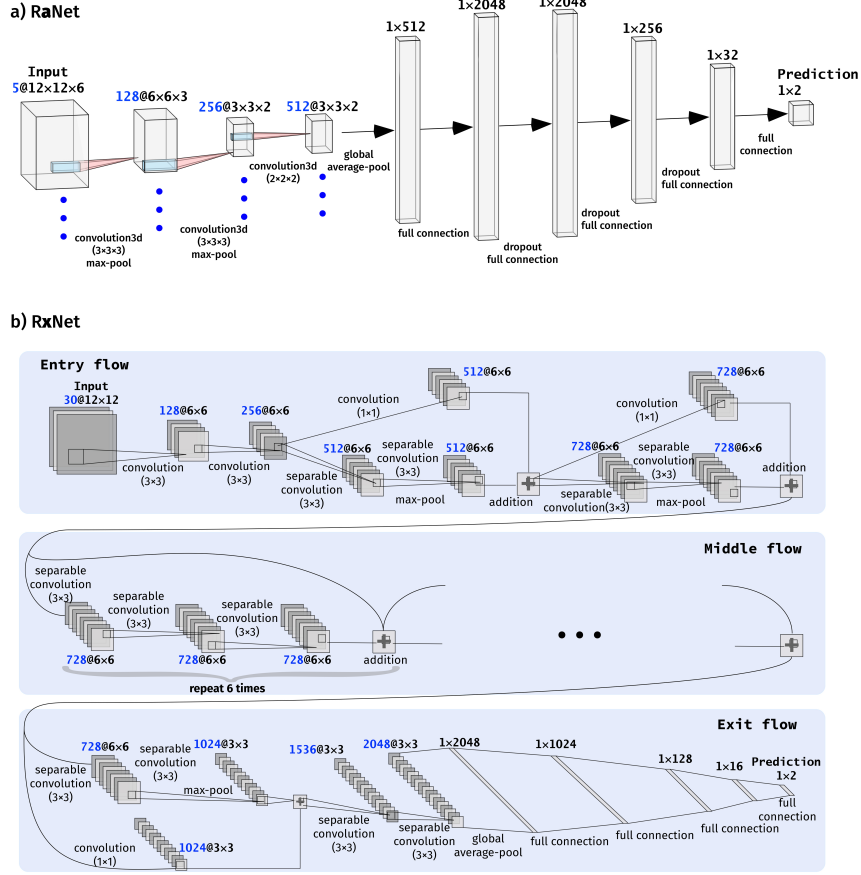


**Figure 1.** Structure of a) RaNet and b) RxNet. RaNet uses three-dimensional filters in the convolutional layers and leaky ReLU activation for all layers; the first two convolutional layers are followed by batch normalization layers which are not shown. RxNet uses two-dimensional filter in its regular convolution and channel-wise separable convolution operations, and used the ReLU activation function for all layers; all convolutional layers are followed by batch normalization layers which are not shown. Blue-font values before @ indicate the number of channels of each layer. The expression after @ indicate the size of activation arrays of a channel. The expression in brackets indicate the size of filters used by convolutional layers.

208  $v$ , and relative humidity as zero. The deviations of variables from base states are defined as  
 209 perturbations and then scaled by their root-mean-square amplitudes. Because RxNet treats  
 210 the data on each pressure level as separate variables, input data of each channel for RxNet  
 211 are simply rescaled to be in the range of  $-1$  to  $1$  using minimum and maximum values.

212 These two CNNs were trained using the 90th percentile to partition data into the cat-  
 213 egories of “extreme” and “non-extreme” rain. Because deep neural networks are expected to  
 214 be more competent than SVMs, we did not use the two-step procedure as in the Dual SVM  
 215 model. These two CNNs were trained with Adam (adaptive moment estimation) optimizer,  
 216 which iterates to minimized the weighted cross-entropy loss function,

$$217 \quad L = -\frac{1}{N} \sum_{i=1}^N \sum_{j=1}^K w_j T_{ij} \log(Y_{ij}). \quad (4)$$

218 where  $T$  is training targets,  $Y$  is predicted probability,  $N$  is the number of instances,  $K$  is  
 219 the number of classes, and  $w$  is the weighting factor. Instead of an unweighted loss function,  
 220 this weighted loss function was used because the number of non-extreme events is much larger  
 221 than that of extremes. The weighting factor  $w$  is set to 0.95 for extreme events and 0.05 for  
 222 the other. Therefore, predicting an extreme event wrong causes a much larger increase in the  
 223 loss function than doing the same to a non-extreme event. RaNet and RxNet were optimized  
 224 with 30 epochs of iteration and a learning rate of  $1 \times 10^{-4}$ . Training them with more iteration  
 225 cycles can increase their accuracy and precision, but leads to deterioration in recall, which  
 226 suggests overfitting and is not favorable for retaining extreme events.

227 For these two CNNs, 60% of the FNL data were used to train the models, and 20% used  
 228 for validation, which helped decide if early stopping was needed during training. The other  
 229 20% data was held out as a test data set for evaluating trained models' performance. 70-15-  
 230 15 partitioning of the train-validation-test data sets was also evaluated and did not cause a  
 231 significant difference in results.

## 232 2.4 Performance Metrics

233 In the training of SVMs and CNNs, algorithms try to achieve the highest classification  
 234 accuracy. However, because extreme events are only a small fraction of the data, accuracy of  
 235 trained models is always intuitively high. Thus, in our discussion, we report the performance  
 236 of trained models primarily with precision and recall. Precision quantifies the skill of a trained  
 237 model in filtering out irrelevant circulation patterns, whereas recall quantifies how well the  
 238 relevant patterns are retained. Specifically,

$$239 P_y^M = \frac{|\{r > r_y\} \cap \{r' > r_y\}|}{|\{r' > r_y\}|}, \quad (5)$$

$$241 R_y^M = \frac{|\{r > r_y\} \cap \{r' > r_y\}|}{|\{r > r_y\}|}, \quad (6)$$

242 where  $P_y^M$  and  $R_y^M$  are precision and recall of the model M when cases with precipitation rates  
 243 greater than the  $y$ -th percentile,  $r_y$ , are labeled as positive.  $r_y$  may *differs* from the actual  
 244 threshold used in labelling data when training M.  $\{r > r_y\}$  represent the set of instances for  
 245 which real rain rate ( $r$ ) exceeds  $r_y$ , and  $\{r' > r_y\}$  is the set of instances for which the model  
 246 M predicts rain rate ( $r'$ ) exceeds  $r_y$ .  $r'$  was not computed by the machine learning models  
 247 explicitly, but rather the condition,  $r' > r_y$ , was judged by the model M.

## 248 3 Results

### 249 3.1 Dual SVM Model

250 Figure 2 shows the performance of the Dual SVM model trained with the data for the  
 251 three cities, HK, MN, and SG. The precision of SVM1 for its training criteria,  $P_{30}^{SVM1}$ , is around  
 252 0.7, and the recall of SVM1 for its training criteria,  $R_{30}^{SVM1}$ , is between 0.48 and 0.59. These  
 253 recall values are not very high. However, if we target to retrieve precipitation event with rain  
 254 rate higher than the 90th and 99th percentiles, we can find that the corresponding recall,  
 255  $R_{90}^{SVM1}$  and  $R_{99}^{SVM1}$ , is between 0.82 and 0.92 for HK and MN, and between 0.69 and 0.79 for  
 256 SG. It should be noted that because we did not include rain rate lower than  $0.05 \text{ mm h}^{-1}$  in  
 257 calculating the percentiles, SVM1 eliminates much more than 30% circulation data from all  
 258 time slices. Precipitation rates in HK, MN, and SG exceed the corresponding 30th percentiles  
 259 only in 14.5%, 28.9%, and 29.4%, respectively, of time slices of the 19 years (not shown).

260 Figure 2 also shows the performance of SVM2 for training criteria, as well as for real  
 261 extreme events defined by the 90th and 99th percentiles. For SG, we were unable to obtain a  
 262 converged solution when the training criterion was set as the 80th percentile. Therefore, it is  
 263 likely that those circulation patterns, responsible for the extreme events defined with the 80th  
 264 percentile, are inseparable from others by an SVM.

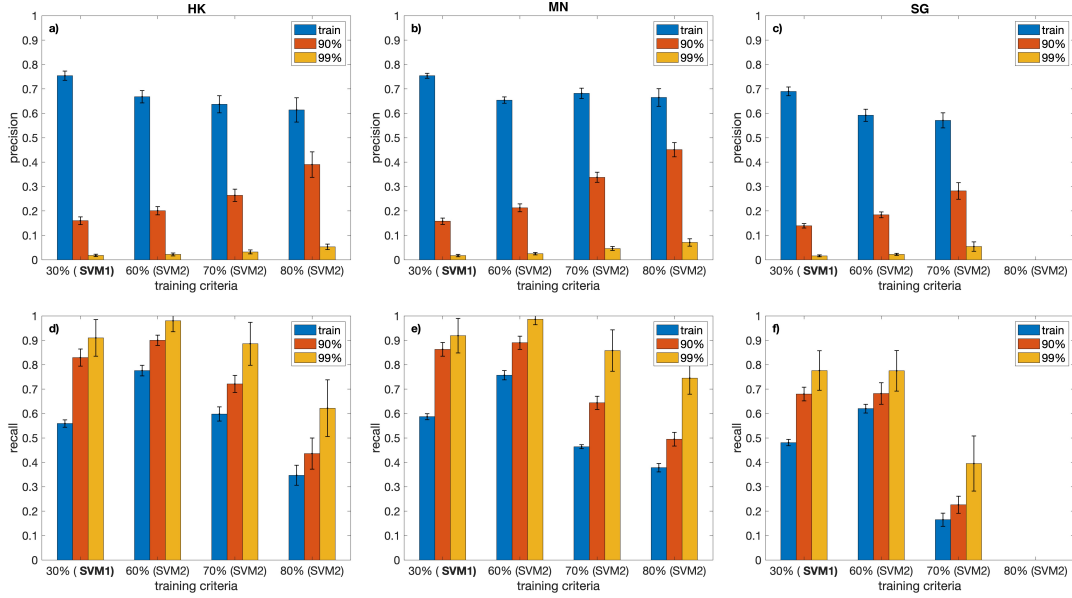


**Figure 2.** Precision (a–c) and recall (d–f) of the trained SVMs. a) and d) are the SVMs for HK, b) and e) for MN, c) and f) for SG. The SVMs were trained for the thresholds indicated below the horizontal axis, but their performance is evaluated against the training criteria and the 90th and 99th percentiles of rain rates.

265 The precision of SVM2 for the 90th and 99th percentiles (red and yellow bars in Fig. 2a–c)  
 266 increases as the training criteria increase to become close to the evaluation criteria. However,  
 267 those values are relatively low because SVM2 was trained with different criteria (e.g., the 70th  
 268 percentile). The recall of SVM2 decreases as the training criteria increases. A higher training  
 269 threshold means that we can filter out more “irrelevant” instances. However, it also increases  
 270 our chance of losing actual extreme events due to misclassification. Based on Fig. 2, the  
 271 SVM2 trained with the 70th percentile of rain rate appears to be the most balanced model  
 272 for applications. If we target to retrieve extreme events defined by the 99th percentile in the  
 273 selection, the SVM1 and the SVM2 trained with the 70th percentile can yield combined recall  
 274 (product of the recall of SVM1 and SVM2) of  $R_{99}^{SVM1} R_{99}^{SVM2} = 0.81, 0.79, \text{ and } 0.31$ , for HK,  
 275 MN, and SG, respectively.

276 The unsatisfactory performance of the Dual SVM model for SG data suggests we cannot  
 277 obtain a very reliable subset of data if we want to study extreme rainfall in deep tropics with  
 278 SVMs. Moreover, because we can only use the 70th percentile of rain rate in the training of  
 279 SVM2, we still need to “waste” a notable fraction of our computation to ensure the SVMs keep  
 280 most extreme events. Can we overcome these difficulties with deep neural networks?

### 281 3.2 Convolutional Neural Networks

282 The performance of RaNet and RxNet is shown in Table 1. For the test set of FNL  
 283 data, the precision of the two CNNs,  $P_{90}^{RaNet}$  and  $P_{90}^{RxNet}$ , is between 0.23 and 0.33, which  
 284 is not very impressive, but their recall,  $R_{90}^{RaNet}$  and  $R_{90}^{RxNet}$ , is high, between 0.75 and 0.92.  
 285 When evaluated for the 99th percentile, the recall of the CNNs,  $R_{99}^{RaNet}$  and  $R_{99}^{RxNet}$ , reaches  
 286 0.93 to 0.98. Those high values contrast with the much lower recall values of the dual SVM  
 287 models, especially for the SG regions. Therefore, the deep neural networks RaNet and RxNet  
 288 are indeed more powerful in recognizing large-scale patterns responsible for extreme events.  
 289 The relative low precision values partially result from the weighted cross-entropy loss, which

**Table 1.** Performance metrics of RaNet and RxNet. Three data sets, FNL, ERA5, and JRA-55, were used to evaluate the models. For FNL, only the test dataset (20% of all) was used to evaluate the performance of trained models, whereas, for ERA5 and JRA-55, entire data sets were used. The rows of “precision” and “recall” are computed for the training threshold, the 90th percentile values. The rows of “recall (99%)” is the recall when the trained models are evaluated for the 99th percentile values. “retention” refers to the fraction of data retained (as relevant to extreme events) by the trained models.

		HK Region		MN Region		SG Region	
		RaNet	RxNet	RaNet	RxNet	RaNet	RxNet
accuracy	FNL	0.936	0.961	0.897	0.933	0.900	0.920
	ERA5	0.948	0.964	0.904	0.938	0.905	0.931
	JRA-55	0.950	0.957	0.907	0.931	0.883	0.926
precision	FNL	0.238	0.331	0.229	0.307	0.230	0.274
	ERA5	0.257	0.326	0.224	0.292	0.201	0.238
	JRA-55	0.259	0.276	0.217	0.241	0.148	0.180
recall	FNL	0.921	0.858	0.832	0.748	0.770	0.749
	ERA5	0.777	0.663	0.725	0.553	0.557	0.428
	JRA-55	0.738	0.645	0.650	0.462	0.475	0.299
recall (99%)	FNL	0.985	0.983	0.955	0.935	0.927	0.936
	ERA5	0.927	0.843	0.904	0.800	0.742	0.643
	JRA-55	0.901	0.798	0.864	0.695	0.622	0.465
retention	FNL	0.082	0.055	0.126	0.084	0.120	0.098
	ERA5	0.064	0.043	0.112	0.065	0.099	0.064
	JRA-55	0.060	0.049	0.104	0.066	0.115	0.059

290 ensures the high values of recall. We trained RaNet with unweighted cross-entropy loss, it  
 291 exhibits precision of 0.38 to 0.49, and recall (for the 90th percentile) drops to 0.58 to 0.67,  
 292 leading to the misclassification of a large number of extreme events.

293 Different climate models potentially have their intrinsic biases, can the CNNs trained with  
 294 FNL data perform well when applied to climate simulation data? To evaluate the tolerance of  
 295 RaNet and RxNet to potential GCM biases, we apply them to another two reanalysis datasets,  
 296 ERA5 and JRA-55, to compute the performance metrics of the FNL-trained CNNs (while still  
 297 using the GPM precipitation to label instances). Different reanalysis data sets are known to  
 298 represent some parts of the general circulation differently (Kossin, 2015). Although we have  
 299 adjusted the mean and amplitude of ERA5 and JRA-55 data (Section 2.1) to correct leading  
 300 order biases, significant changes in the performance of trained CNNs can still be found when  
 301 applied to the ERA5 and JRA-55 data.

302 In Table 1, application of the FNL-trained CNNs to ERA5 data does not result in a large  
 303 decrease in the accuracy and precision, but leads to a sharp drop in the recall, especially for  
 304 the SG region. The recall corresponding to the training criterion (90th percentile) for the SG  
 305 region is around 0.76 for the FNL test data set but drop to 0.56 and 0.43 for RaNet and RxNet,  
 306 respectively, for the ERA5 data. When considering the 99th percentile,  $R_{99}^{\text{RaNet}}$  and  $R_{99}^{\text{RxNet}}$  are  
 307 higher than 0.80 for the HK and MN regions with the ERA5 data, but show recall of 0.74 and  
 308 0.64, respectively, for the SG region.

309 The JRA-55 data set appears to differ from the FNL data even more than the ERA5 data.  
 310 Recall values of RaNet and RxNet, when applied to the JRA-55 data, becomes even lower  
 311 than those for ERA5. For the HK region, the recall  $R_{99}^{\text{RaNet}}$  and  $R_{99}^{\text{RxNet}}$  are 0.90 and 0.80,  
 312 respectively, with the JRA-55 data, which are still satisfactory. However for the SG region,

313  $R_{99}^{\text{RaNet}}$  and  $R_{99}^{\text{RxNet}}$  are only 0.62 and 0.47, respectively, with the JRA-55 data. These results  
 314 suggest that if the CNNs are trained with one circulation data set and applied to deep tropics  
 315 in climate simulations, they may not capture all the extreme events that can potentially be  
 316 generated by the circulation patterns in climate models.

317 Overall, RxNet exhibits higher accuracy and precision than RaNet for all three regions.  
 318 However, RaNet exhibits higher recall values and appears to be more resilient to potential  
 319 model biases. For example,  $R_{99}^{\text{RaNet}}$  is consistently higher than  $R_{99}^{\text{RxNet}}$  by more than 0.10 in all  
 320 three regions. However, the relatively higher recall comes with a price in computational cost,  
 321 that is, less “irrelevant” data can be filtered out if the recall needs to be high. For example,  
 322 when using ERA5 data for the MN region, RaNet retains twice as much data as RxNet.

## 323 4 Discussion and Summary

324 In this study, we demonstrated that the SDD of extreme rainfall is viable through the  
 325 use of deep neural networks. For the subtropical region, this methodology appears to be very  
 326 robust. The trained CNNs performed well even when different reanalysis data sets were used to  
 327 evaluate their performance, and 92% to 96% of circulation data can be filtered out as irrelevant  
 328 patterns for extreme events in the HK region. For deep tropics, the methodology is still useful  
 329 but appears to be not highly reliable (at least for the CNNs we tested here). The trained  
 330 CNNs performed well for the FNL data, which was used to train them. However, performance  
 331 deteriorates when different reanalysis data sets were used in evaluation, especially for the SG  
 332 region with JRA-55 data.

333 From simple SVMs to sophisticated CNNs, the model performance is always worse for  
 334 the SG region than the other two regions. We speculate this is because the link between  
 335 large-scale circulation and local precipitation in deep tropics is just not as strong as those in  
 336 subtropics.  $k$ -medoid clustering analysis (Supplementary Figure S4-S6) suggests that extreme  
 337 precipitation events in the HK region are typically associated with warm-sector convection,  
 338 frontal rainfall, and tropical cyclones (Fig. S4), of which the first type comprises the majority  
 339 (Wu et al., 2020). Those weather patterns have distinct large-scale features. In contrast, ex-  
 340 treme precipitation appears to be connected with squall lines and cold pools for the SG regions  
 341 (Porson et al., 2019), which exhibit significant variability at smaller grid scales (Fig. S6). It  
 342 is probably not surprising that fitting small-scale features is more complicated than fitting  
 343 large-scale ones.

344 Therefore, the SDD of extreme precipitation in deep tropics appears to be challenging.  
 345 Including multiple reanalysis data when training CNNs might alleviate the problem of overfit-  
 346 ting (low tolerance to potential model biases). Using a model structure with an intermediate  
 347 level of sophistication, like the RaNet here, may also help. In subtropical regions, the potential  
 348 of advanced deep neural networks, such as RxNet here, can be fully exploited to reduce com-  
 349 putational expense while confidently retaining the majority of the circulation patterns causing  
 350 extreme rainfall. In our study, the recall  $R_{99}^{\text{RxNet}} \geq 0.80$  for the HK region with all circulation  
 351 data sets. It is the next step for our research to apply deep neural networks to SDD of climate  
 352 simulations and explore the response of extreme rainfall to global warming.

## 353 Acknowledgments

354 The author thanks two anonymous reviewers for valuable comments and acknowledges the  
 355 support of the Research Grants Council of Hong Kong SAR, China (Project No. AoE/E-603/18  
 356 and HKUST 26305720). FNL and JRA-55 data was obtained from the Research Data Archive  
 357 at the National Center for Atmospheric Research, Computational and Information Systems Lab-  
 358 oratory (<https://rda.ucar.edu/>). The ERA5 data set was provided through Copernicus Climate  
 359 Change Service Climate Data Store (<https://cds.climate.copernicus.eu/>) The GPM IMERG  
 360 precipitation data was provided by the Goddard Earth Sciences Data and Information Services  
 361 Center (GES DISC) (<https://doi.org/10.5067/gpm/imerq/3b-hh/06>).

362 **References**

- 363 Agel, L., Barlow, M., Feldstein, S. B., & Gutowski, W. J. (2018). Identification of large-scale  
 364 meteorological patterns associated with extreme precipitation in the us northeast. *Clim.*  
 365 *Dynam.*, *50*(5–6), 1819–1839.
- 366 Brenowitz, N. D., & Bretherton, C. S. (2019). Spatially extended tests of a neural network  
 367 parametrization trained by coarse-graining. *J. Adv. Model. Earth Syst.*, *11*(8), 2728–2744.
- 368 Chattopadhyay, A., Nabizadeh, E., & Hassanzadeh, P. (2020). Analog forecasting of extreme-  
 369 causing weather patterns using deep learning. *J. Adv. Model. Earth Syst.*, *12*(2),  
 370 e2019MS001958.
- 371 Chollet, F. (2017). Xception: Deep learning with depthwise separable convolutions. In *Proceed-*  
 372 *ings of the IEEE conference on computer vision and pattern recognition* (pp. 1251–1258).
- 373 Conticello, F., Cioffi, F., Merz, B., & Lall, U. (2018). An event synchronization method to link  
 374 heavy rainfall events and large-scale atmospheric circulation features. *Int. J. Climatol.*,  
 375 *38*(3), 1421–1437.
- 376 Copernicus Climate Change Service. (2017). *ERA5: Fifth generation of ecmwf atmospheric*  
 377 *reanalyses of the global climate*. Copernicus Climate Change Service Climate Data Store  
 378 (CDS). Retrieved from <https://cds.climate.copernicus.eu>
- 379 Cristianini, N., Shawe-Taylor, J., et al. (2000). *An introduction to support vector machines and*  
 380 *other kernel-based learning methods*. Cambridge University Press.
- 381 Gagne, D. J., Christensen, H. M., Subramanian, A. C., & Monahan, A. H. (2020). Machine  
 382 learning for stochastic parameterization: Generative adversarial networks in the lorenz'96  
 383 model. *J. Adv. Model. Earth Syst.*, *12*(3), e2019MS001896.
- 384 Haarsma, R. J., Roberts, M. J., Vidale, P. L., Senior, C. A., Bellucci, A., Bao, Q., ... others  
 385 (2016). High resolution model intercomparison project (highresmip v1. 0) for cmip6.  
 386 *Geosci. Model Dev.*, *9*(11), 4185–4208.
- 387 Han, L., Sun, J., Zhang, W., Xiu, Y., Feng, H., & Lin, Y. (2017). A machine learning nowcasting  
 388 method based on real-time reanalysis data. *J. Geophys. Res.*, *122*(7), 4038–4051.
- 389 Huffman, G., Stocker, E., Bolvin, D., Nelkin, E., & Jackson, T. (2019). *GPM IMERG Final*  
 390 *Precipitation L3 Half Hourly 0.1 degree × 0.1 degree V06, Greenbelt, MD, Goddard*  
 391 *Earth Sciences Data and Information Services Center (GES DISC)*. doi: 10.5067/GPM/  
 392 IMERG/3B-HH/05
- 393 Japan Meteorological Agency. (2013). *JRA-55: Japanese 55-year reanalysis, daily 3-hourly*  
 394 *and 6-hourly data*. Boulder CO: Research Data Archive at the National Center for  
 395 Atmospheric Research, Computational and Information Systems Laboratory. Retrieved  
 396 from <https://doi.org/10.5065/D6HH6H41>
- 397 Kalnay, E., Kanamitsu, M., Kistler, R., Collins, W., Deaven, D., Gandin, L., ... others (1996).  
 398 The ncep/ncar 40-year reanalysis project. *Bull. Amer. Meteor. Soc.*, *77*(3), 437–472.
- 399 Kendon, E. J., Ban, N., Roberts, N. M., Fowler, H. J., Roberts, M. J., Chan, S. C., ... Wilkinson,  
 400 J. M. (2017). Do convection-permitting regional climate models improve projections of  
 401 future precipitation change? *Bull. Amer. Meteor. Soc.*, *98*(1), 79–93.
- 402 Kendon, E. J., Roberts, N. M., Fowler, H. J., Roberts, M. J., Chan, S. C., & Senior, C. A. (2014).  
 403 Heavier summer downpours with climate change revealed by weather forecast resolution  
 404 model. *Nature Clim. Change*, *4*(7), 570–576.
- 405 Knighton, J., Pleiss, G., Carter, E., Lyon, S., Walter, M. T., & Steinschneider, S. (2019).  
 406 Potential predictability of regional precipitation and discharge extremes using synoptic-  
 407 scale climate information via machine learning: An evaluation for the eastern continental  
 408 united states. *J. Hydrometeor.*, *20*(5), 883–900.
- 409 Kossin, J. P. (2015). Validating atmospheric reanalysis data using tropical cyclones as ther-  
 410 mometers. *Bull. Amer. Meteor. Soc.*, *96*(7), 1089–1096.
- 411 Krizhevsky, A., Sutskever, I., & Hinton, G. E. (2012). Imagenet classification with deep con-  
 412 volutional neural networks. In *Advances in neural information processing systems* (pp.  
 413 1097–1105).
- 414 Li, J., Chen, H., Rong, X., Su, J., Xin, Y., Furtado, K., ... Li, N. (2018). How well can a climate  
 415 model simulate an extreme precipitation event: A case study using the transpose-amip  
 416 experiment. *J. Climate*, *31*(16), 6543–6556.

- 417 McGovern, A., Elmore, K. L., Gagne, D. J., Haupt, S. E., Karstens, C. D., Lagerquist, R., ...  
418 Williams, J. K. (2017). Using artificial intelligence to improve real-time decision-making  
419 for high-impact weather. *Bull. Amer. Meteor. Soc.*, *98*(10), 2073–2090.
- 420 NCEP/NWS/NOAA. (2000). *NCEP FNL operational model global tropospheric analyses,*  
421 *continuing from July 1999*. Boulder CO: Research Data Archive at the National Center  
422 for Atmospheric Research, Computational and Information Systems Laboratory. Retrieved  
423 from <https://doi.org/10.5065/D6M043C6>
- 424 Nie, J., Shaevitz, D. A., & Sobel, A. H. (2016). Forcings and feedbacks on convection in the  
425 2010 Pakistan flood: Modeling extreme precipitation with interactive large-scale ascent.  
426 *J. Adv. Model. Earth Syst.*, *8*(3), 1055–1072. doi: 10.1002/2016MS000663
- 427 O’Gorman, P. A., & Schneider, T. (2009). The physical basis for increases in precipita-  
428 tion extremes in simulations of 21st-century climate change. *Proc. Natl. Acad. Sci.*  
429 *USA*, *106*(35), 14773–14777. Retrieved from [https://www.pnas.org/content/106/](https://www.pnas.org/content/106/35/14773)  
430 [35/14773](https://www.pnas.org/content/106/35/14773) doi: 10.1073/pnas.0907610106
- 431 Porson, A. N., Hagelin, S., Boyd, D. F., Roberts, N. M., North, R., Webster, S., & Lo, J. C.-F.  
432 (2019). Extreme rainfall sensitivity in convective-scale ensemble modelling over Singa-  
433 pore. *Quart. J. Roy. Meteor. Soc.*, *145*(724), 3004–3022.
- 434 Prein, A. F., Langhans, W., Fosser, G., Ferrone, A., Ban, N., Goergen, K., ... others (2015). A  
435 review on regional convection-permitting climate modeling: Demonstrations, prospects,  
436 and challenges. *Rev. Geophys.*, *53*(2), 323–361.
- 437 Rainaud, R., Brossier, C. L., Ducrocq, V., & Giordani, H. (2017). High-resolution air-sea  
438 coupling impact on two heavy precipitation events in the western Mediterranean. *Quart.*  
439 *J. Roy. Meteor. Soc.*, *143*(707), 2448–2462.
- 440 Sachindra, D., Ahmed, K., Rashid, M. M., Shahid, S., & Perera, B. (2018). Statistical down-  
441 scaling of precipitation using machine learning techniques. *Atmos. Res.*, *212*, 240–258.
- 442 Van Der Wiel, K., Kapnick, S. B., Vecchi, G. A., Cooke, W. F., Delworth, T. L., Jia, L., ... Zeng,  
443 F. (2016). The resolution dependence of contiguous US precipitation extremes in response  
444 to CO<sub>2</sub> forcing. *J. Climate*, *29*(22), 7991–8012.
- 445 Weyn, J. A., Durran, D. R., & Caruana, R. (2019). Can machines learn to predict weather? using  
446 deep learning to predict gridded 500-hPa geopotential height from historical weather  
447 data. *J. Adv. Model. Earth Syst.*, *11*(8), 2680–2693.
- 448 Wu, N., Ding, X., Wen, Z., Chen, G., Meng, Z., Lin, L., & Min, J. (2020). Contrasting frontal  
449 and warm-sector heavy rainfalls over South China during the early-summer rainy season.  
450 *Atmospheric Research*, *235*, 104693.